7

Application of near-surface geophysical methods for imaging active faults in the Himalaya

Dowchu DRUKPA[1], Stéphanie GAUTIER[2] and Rodolphe CATTIN[2]
[1] *Earthquake & Geophysics Division, Department of Geology & Mines, Thimphu, Bhutan*
[2] *University of Montpellier, Montpellier, France*

Introduction

Near-surface geophysical investigation is a relevant tool to provide quantitative constraints of the nature and the geometry of shallow fault zones. The strategy consists of combining results coming from different geophysical methods, including electrical resistivity, seismic and gravity measurements, to obtain a detailed characterization of the first 100s of m in terms of geometry (faults, stratigraphy, buried markers), cumulative deformation on the downthrow, and quantification of the physical parameters around the fault. Integrating the new constraints on fault geometry and geomorphological and regional geodetic information allows one to estimate fault slip rate and to identify potential slip partitioning between horizontal and vertical displacement. The characterization of the seismic sources and slip partitioning has major implications in seismic hazard evaluation in the Himalaya area.

Himalaya, dynamics of a giant,
coordinated by Rodolphe CATTIN and Jean-Luc EPARD.

7.1. Near-surface geophysics

Geophysical methods have been widely used for the characterization of subsurface tectonic features (Suzuki et al. 2000 ; Demanet et al. 2001 ; Morandi, Ceragioli 2002 ; Louis et al. 2002 ; Wise et al. 2003 ; Nguyen et al. 2005, 2007 ; Kaiser et al. 2009). Depending on the scale of investigation, geophysical methods can be divided into two categories (Mussett et al. 2000): deep surveys, with penetration depth ranges from 100 m to several km, which are mainly used to define regional seismotectonic models and, near-surface surveys which image structures at shallow depth (0-200 m) such as fault systems, lithological interfaces, landslide bodies as well as cumulative deformation. The same near-surface geophysical techniques are also deployed to quantify groundwater resources, to monitor active geohazards, for archeogeophysical exploration and geotechnical site characterization (Telford et al. 1990 ; Reynolds 1997). The success of any geophysical investigation is dependent on several factors, including

– the presence of strong contrasts in terms of physical properties,

– the availability of geological, geomorphological or hydrological information,

– practical aspects for the deployment such as topography or site accessibility.

Having good *a priori* information is critically important to choose relevant locations for the surveys and validate the geophysical investigations' outcome.

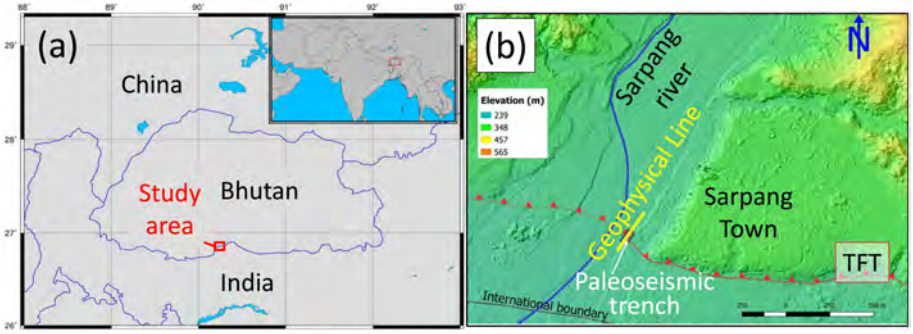

Figure 7.1. *(a) Location of the Kingdom of Bhutan and the study area in south Central part of Bhutan. (b) High resolution Digital Elevation model (DEM) from satellite image of the study area showing the Topographic Frontal Thrust (TFT) fault trace, the location of the paleoseismic trench studied by Le Roux-Mallouf et al. (2016) and our geophysical profile (yellow line).*

Various near-surface geophysical methods are particularly adapted to image internal structures and physical properties of fault zones, in a depth range between a few meters to a hundred meters (Demanet et al. 2001 ; Villani et al. 2015). In particular,

geophysical data can contribute to characterizing the geometry of the fault dip angle, the thickness of quaternary layers, and possible offsets at shallow depths. Those data can also help detect blind faults close to the surface and find the appropriate location for trench excavations. Despite promising results on many fault zones around the world (Nguyen 2005), near-surface geophysical investigations have been little implemented in the Himalayas.

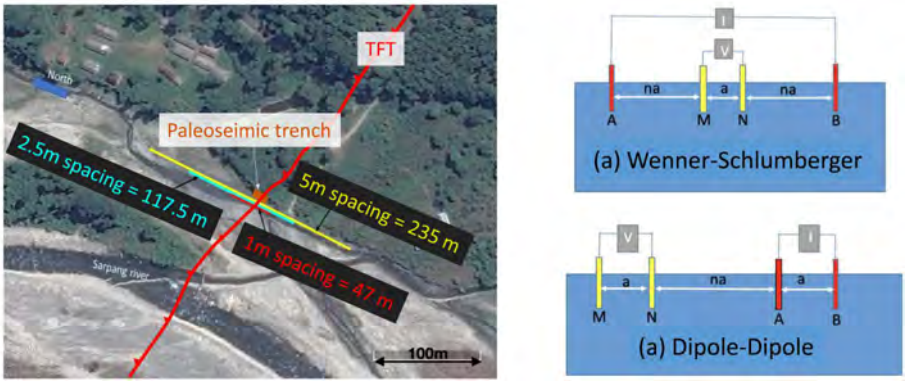

Figure 7.2. *Location of both the Electrical Resistivity Tomography (ERT) surveys (yellow, blue, and red lines for the 5 m, 2.5 m and 1 m electrode spacing soundings, respectively) and the paleoseismic trench in Sarpang site (left) and geometric configurations used in the study (right).*

In this framework, near-surface geophysical investigations were carried out in central southern Bhutan for shallow subsurface imaging of the Topographic Frontal Thrust (Figure 7.1). At the front, *a priori* information of the exact location and estimated dip angle of the fault on the surface were gathered from previous geomorphological and paleoseismological studies (Berthet et al. 2014 ; Le Roux-Mallouf et al. 2016). Observations in the paleoseismic trench also confirmed rheological contrasts, suggesting strong physical parameters variations as usually described in fault zones (Boness, Zoback 2004 ; Hung et al. 2009 ; Jeppson et al. 2010), which are in favor of geophysical imaging. Further, the case study site is located in the foothills, characterized by low elevation variations. This specific geographic feature ensures easy accessibility and feasibility of surveys. Geophysical data for the case study site is acquired along the east side of Sarpang river, where the east-west trending TFT trace was intersected by the previous paleoseismic trench study down to 1 m depth (Figure 7.1). Using various geophysical methods (Electrical resistivity tomography (ERT), seismic refraction, and gravity measurements) provides images of different physical properties at different depths of investigation. All geophysical data were collected along the same N-S profile, with varying lengths of spread depending on the methods. The midpoints of

the geophysical surveys were positioned at the fault location at the surface deduced from the paleoseismic study.

7.1.1. *Geophysical methods for fault mapping*

Electrical resistivity tomography (ERT)

Low resistivity materials generally characterize fault zones. Hence, electrical resistivity tomography is widely used for near-surface fault imaging (Phillips, Kuckes 1983). To obtain well-resolved images close to the surface as well as the deeper depth of investigation, combining ERT profiles with different electrode spacing is recommended (Nguyen et al. 2005 ; Gelis et al. 2010). Among the different geometric configurations available for ERT surveys, the commonly used Wenner-Schlumberger (WS) and Dipole-Dipole (DD) configurations (Figure 7.2) appears to achieve a good compromise between vertical and horizontal resolution and effect of noise (Dahlin, Zhou 2004 ; Loke 2015).

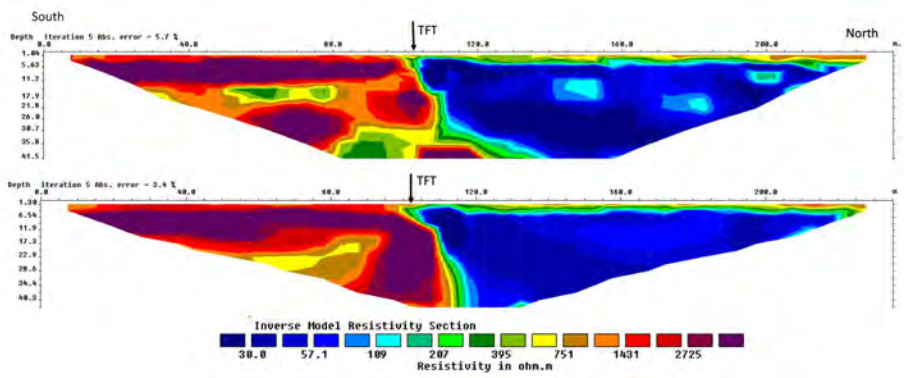

Figure 7.3. *2D 5m-spacing Dipole-Dipole ERT model (top) and Wenner-Schlumberger model (bottom) inverted with* RES2DINV *(Loke, Barker 1996). Both images represent models obtained after 5 iterations. The RMS corresponds to the misfit between observed and computed data. The TFT label indicates the location of fault.*

Accordingly, in south Bhutan, both WS and DD electrical resistivity soundings, with three different electrode spacings (1, 2.5, and 5 m), were carried out (Drukpa et al. 2017). The topography along the profile is relatively smooth, with variations less than 1.3 m. Therefore, no topographic correction was necessary for resistivity data analyses. The obtained ERT inverted sections (Figure 7.3) illustrate that an electrical resistivity survey is a valuable tool for characterizing faults in superficial layers from

the ground surface. The different surveys provided consistent results. The WS electrical images appear to be more robust because of a greater sensitivity to both lateral and vertical variations (Nguyen et al. 2007). These resistivity images point out a major sub-vertical discontinuity, which is consistent with the prolongation of the fault towards the surface. More precisely, the fault zone is marked by high electrical resistivity contrasts ($\sim$1:100) with a nearly vertical contact down to $\sim$40 m depth. The north side shows a uniform apparent resistivity layering with a thin upper layer resistivity of 200-1000 Ω·m overlying a very low resistivity layer $<$ 100 Ω·m. The south side shows relatively constant resistivity values (1000-4000 Ω·m) with a very high resistivity zone located at 5-15 m depth at the southern end of our profile. A thin upper layer of low resistivity is also observed southward.

Seismic tomography

The passive seismic tomography technique is an additional method for characterizing near-surface fault zone (Demanet et al. 2001 ; Villani et al. 2015) by usually estimating P-wave velocity models from traveltimes (see volume 1 – chapter 4). Like ERT, data acquisition layout design for seismic tomography should obtain high-resolution images and achieve the target depth of investigation. These targets can be achieved by maintaining appropriate receiver spacing and roll-along where ever needed to increase the spread length and, therefore deeper depth of investigation.

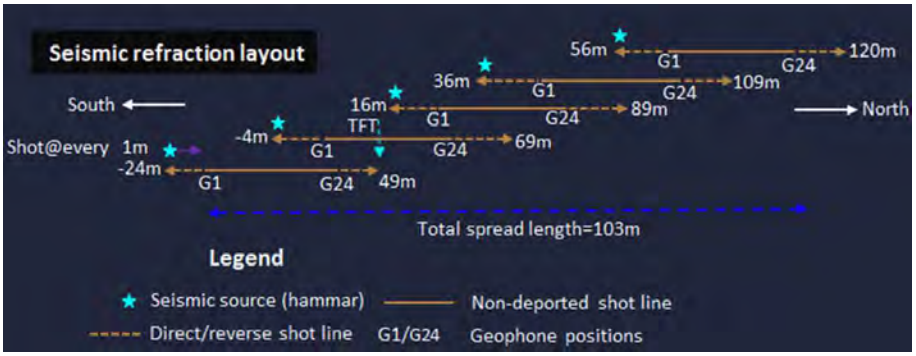

Figure 7.4. *Seismic data acquisition layout plan.*

A seismic survey colocated with ERT profiles was carried out for the case study. It is composed 1 m receiver spacing and five roll-along (shift of 20 geophones and overlap of 4 geophones each time) to finally acquire a 103 m long seismic profile (Figure 7.4) (Drukpa et al. 2017). Seismic sources were generated by hitting a 10 kg sledgehammer on an iron plate at each geophone along each seismic line. A total of 5760 first-arrivals travel times were manually hand-picked (Figure 7.5). As for ERT, no topographic correction was implemented. Seismic refraction images show that the

TFT fault implies an abrupt transition of the traveltimes resulting in a strong constrast of both the ray distribution and the velocity values (Figure 7.5). The velocity model confirms the presence of a shallow interface on the northern side.

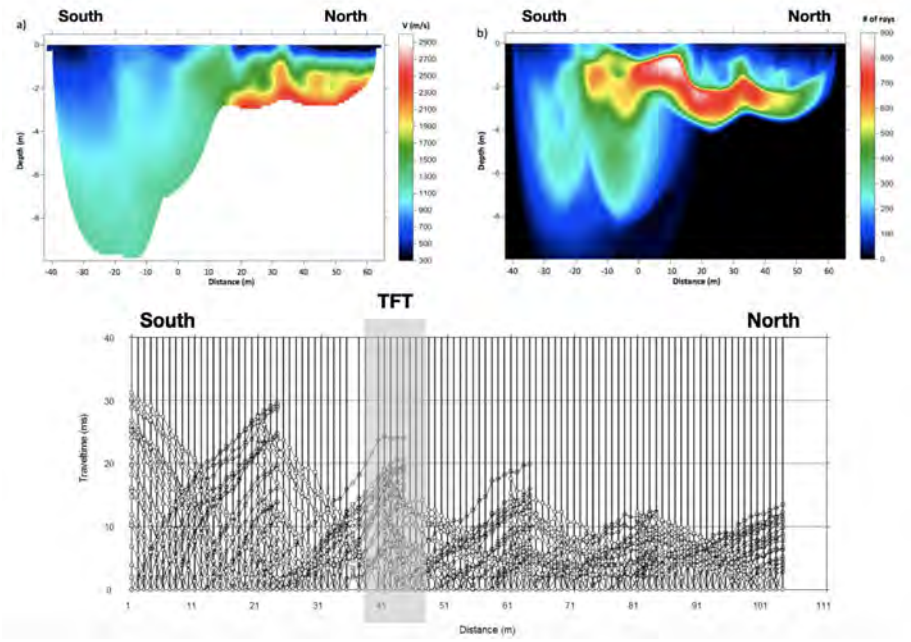

Figure 7.5. *Top: a) Seismic tomographic refraction image showing the velocity variations of the both sides of the TFT obtained using* RAYFRACT *software; The TFT fault trace is located at 0 m. b) Ray coverage illustrating the resolved area. Bottom: Hodochrones of the traveltimes along the seismic line.*

Microgravity

The gravity method is a versatile geophysical technique to determine density contrasts within the Earth. Variations of the gravitational field due to the density contrasts are measured using extremely sensitive instruments to identify anomalies at depth. This technique allows determining and locating the presence of a deficit or an excess of mass in the subsurface, which corresponds to negative or positive anomalies (see volume 1 – chapter 5). In near-surface geophysics, microgravimetry is carried out for various investigations such as detection of karsts and voids, measurements of sediment thickness, archaeological surveys or mineral exploration (Telford et al. 1990).

In southern Bhutan, gravity measurements were recorded along the same South-North profile as the ERT and seismic lines (Drukpa et al. 2017). From the center point

of the survey line positioned at the paleoseismic trench, gravity readings were acquired at every 5 m on either side of the profile covering a distance of 30 m and 105 m to the south and the north, respectively. Spatially denser gravity points were collected in the vicinity of the fault area. Using the GravProcess software (Cattin et al. 2015), network adjustment was performed and topographic effect was corrected from accurate elevation data gathered along the same profile assuming a constant density of 2,670 kg/m^3. A regional trend of -1.58 μGal/m obtained by (Hammer et al. 2013) is also taken into account. The final dataset consists of 139 corrected gravity measurements, which highlight variations along the profile (Figure 7.6). No change at the fault trace is observed, but a transition occurs at around 27 m north of the fault. The southern part of the profile is characterized by a moderate northward increase of ca. 4 μGal/m. The northern part shows an increase twice as large with a northward increase of ca. 450 μGal at 65 m.

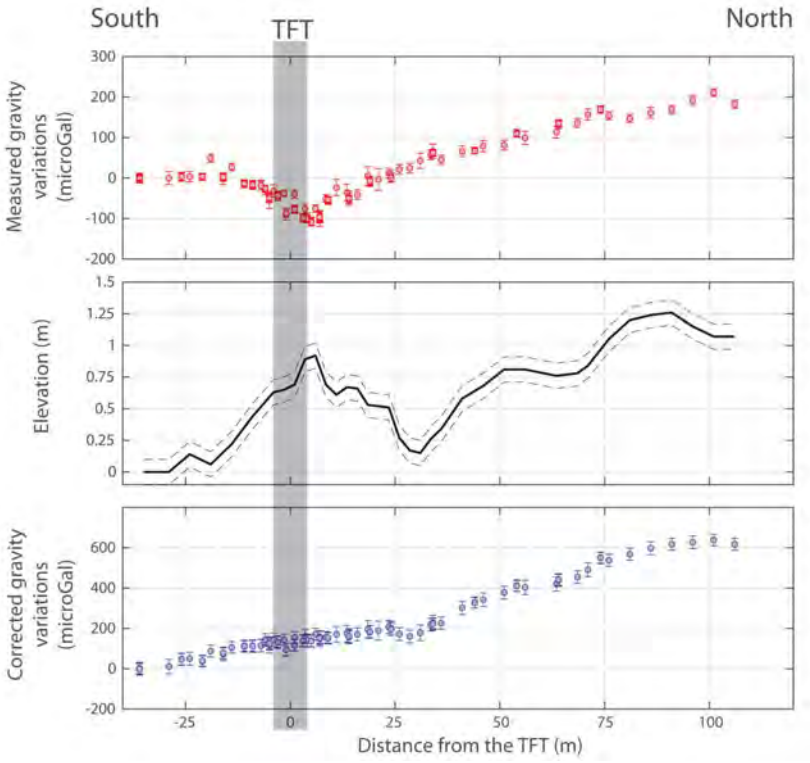

Figure 7.6. *Measured gravity (top), elevation (middle) and gravity variations corrected for both topographic effect and regional trend (bottom) along the study profile. Data uncertainties associated with both accuracy of the CG5 gravimeter and error in elevation measurement.*

7.1.2. *Case study data and inversion technique*

Geophysical inversion is a mathematical and statistical tool used to recover physical properties models from field observations and information on geological structures (Tarantola 2005). Inversion methods can be divided into deterministic and stochastic approaches. Deterministic inversion is a conventional linear approach that consists in gradually updating the model parameters to minimize the differences between observed and theoretical data computed inside the output model (Ellis, Oldenburg 1994). It is a model-driven inversion approach, relatively easy to implement. Still, strong *a priori* constraints are required to converge towards the best acceptable model. Unlike the deterministic approach (Ramirez et al. 2005), the stochastic inversion is a statistical process in which prior information and forward modeling are combined to produce different output models consistent with the available data. This approach provides a more complete description of the possible acceptable solutions but can be time-consuming. In this framework, Drukpa et al. (2017) propose a novel common stochastic approach to invert the near-surface geophysical data. Following Mosegaard & Tarantola (1995), a Markov Chain Monte Carlo technique is used to pseudo-randomly generate a large collection of models according to the posterior probability distribution.

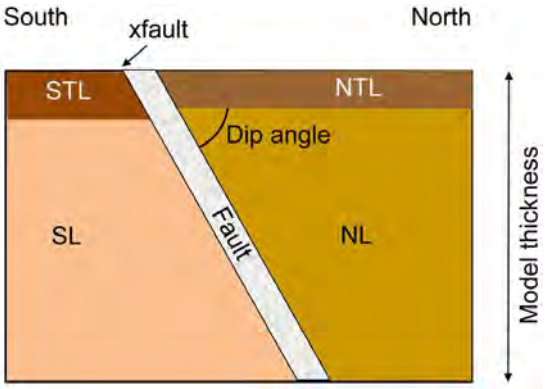

Figure 7.7. *Geometry of the model used in the stochastic inversion. STL - South Top layer, NTL - North Top Layer, SL - South Layer and NL - North Layer. xfault is the prior location of the fault as observed in the field. Model thickness is associated with the thickness investigated by each geophysical method.*

This approach was applied to shallow geophysical data for the case study site in South Bhutan. Assuming a simplified geometry (Figure 7.7), each model is associated with only five bodies, including a south (STL) and north (NTL) top layers, a south (SL) and north (NL) shallow layers and a fault layer. Based on this formulation, a

set of models results for a given dataset combines ten parameters estimations that include either the velocity, the resistivity, or the density of each body, as well as the thickness of layers, the fault location, and the fault dip angle. In order to fix the limit of the solution-space, *a priori* parameters ranges for resistivity and velocity values are obtained from preliminary deterministic inversion using RES2DINV (Loke, Barker 1996) and RAYFRACT (Schuster 1993 ; Sheehan et al. 2005 ; Pasquet et al. 2015), respectively. Assuming prior density contrasts between NL and the other bodies in the -500 to 500 kg/m^3. Concerning the geometry, prior information comes from structural and geomorphological observations (Long et al. 2011 ; Le Roux-Mallouf et al. 2016), which yield top layers thickness less than 5 m and a fault dip angle between 10° and 80°.

The pseudo-random walk through this multi-dimensional parameters space is controlled by the following rules for the transition between model m_i to model m_j :

1) If $L(m_j) \geq L(m_i)$ then accept the proposed transition from i to j.

2) If $L(m_j) < L(m_i)$ then accept the proposed transition from i to j with the probability $\frac{L(m_j)}{L(m_i)}$,

where $L(m_i)$ and $L(m_j)$ are the likelihood of the old and the new model, respectively. Here we assume that the likelihood function can be written as

$$L(m_i) = \exp\left(-\frac{1}{n_{obs}} \sum_{n=1}^{n_{obs}} \frac{|calc_n(m_i) - obs_n|}{\sigma_n}\right), \qquad [7.1]$$

where n_{obs} is the number of data points, obs is the data vector, and σ is the total variance, i.e. the uncertainties associated with each data point. $calc(m_i)$ is the forward modeling function associated with the model m_i. This function is obtained using the different forward modeling depending on the considered datasets described below.

Two-dimensional geoelectrical modeling is performed with the software package R2 (Binley, Kemna 2005 ; Binley 2015). The current flow between electrodes is obtained using a quadrilateral mesh with an exponentially increasing node at depth and a constant node spacing in the horizontal direction. For seismic refraction, synthetic travel times are computed using the real receiver-shot configuration and solving the Eikonal equation with a finite-difference algorithm (Podvin & Lecomte 1991). Rays are traced in the obtained time field with the a posteriori time-gradient method. More precise travel times are then estimated along ray paths (Priolo et al. 2012). The model is discretized on a regular grid. The velocity field is parametrized by trilinear interpolation between grid nodes. Gravity variations along the profile are calculated from the 2D formulations of Won & Bevis (1987), which provide the gravitational acceleration due to n-sided polygons. Here the polygons are associated with the geometry of

the fives bodies described above. The model is extended southward and northward to avoid edge effects at the two terminations.

The posterior probability of each model parameter is then obtained from the final collection of the 5×10^5 sampled models. Compared to the commonly deterministic approach, which leads to the more acceptable model, the main advantages of stochastic inversion include its ability (1) to assess the fault geometry because no smoothing is applied, (2) to provide a measurement of the uncertainties on the obtained dip angle and (3) to allow the study of trade-off analysis between geometric and either electrical resistivity, velocity or density properties. Using parallelism, the computation time associated with electrical, seismic, and gravity inversion on a ten-core workstation is between ca. 10 and 24.5 hours.

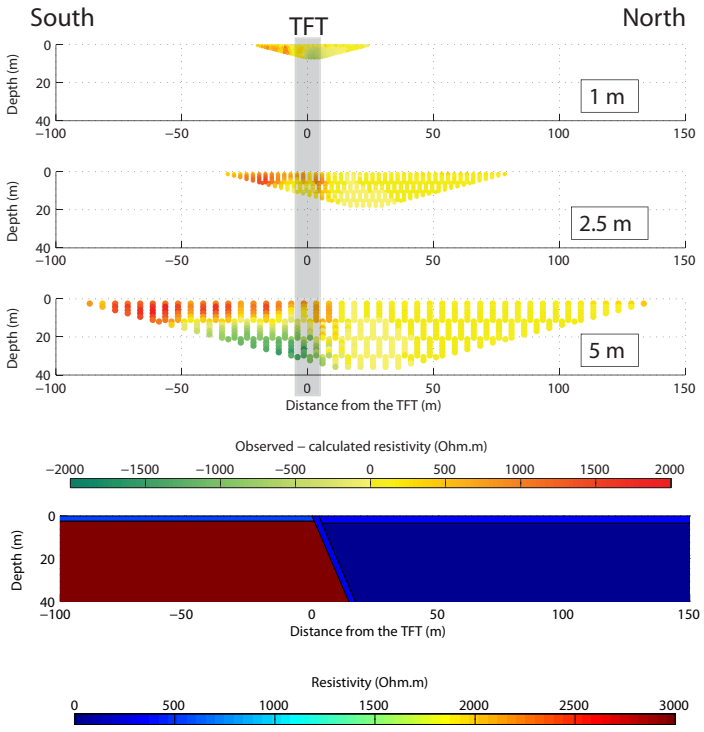

Figure 7.8. *Misfit between observed and calculated ERT pseudo-sections for electrode spacing of 1 m, 2.5 m and 5 m using WS configuration. This misfit is defined as the difference between the observed and calculated resistivities using the electrical model plotted at the bottom.*

7.2. Geophysical results of case study from south Bhutan

7.2.1. *Electrical resistivity tomography*

All Dipole-dipole and Wenner-Schlumberger data were separately inverted using the stochastic approach. The set of most likely models derived from the stochastic approach explains the main features of the observed apparent resistivity pattern, except southward where some residual differences persist (Figure 7.8). It points out a high fault dip angle of ca. 70° (Figure 7.8). Bivariate frequency histograms indicate no tradeoff between dip angle and the other geometric and electrical parameters. This figure constrains the model parameters and discusses the robustness and relevance of the results.

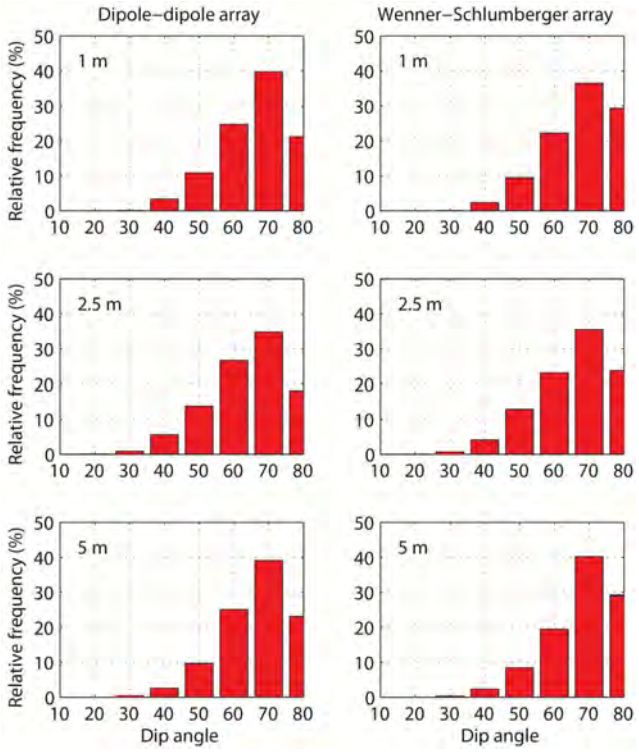

Figure 7.9. *Distribution of TFT dip angle from ERT sections using both dipole-dipole and Wenner-Schlumberger arrays. Electrode spacing ranges from 1 m (top) to 5 m (bottom).*

In southern Bhutan, the histograms suggest a 2.5 m thick fault zone. However, the resistivity of this unit remains poorly resolved. The inversion approach images thin low-resistive top layers, both on the southern ($\sim$2.5 m, $\sim$550 Ω·m) and northern sides ($\sim$3.5 m, $\sim$350 Ω·m). The small resistivity contrasts between those two top layers can prevent the estimation of the fault geometry at a very shallow depth (< 5 m). On the contrary, due to the very high resistivity contrast between the two deeper bodies (SL$\sim$3300 Ω·m vs. NL$\sim$30 Ω·m), we consider the obtained fault dip angle as a well-constrained parameter down to 40 m depth. This assumption is confirmed by the narrow posterior distribution obtained for dip angle. Finally, some discrepancies between the observed and calculated pseudo-sections on the south part. Based on the simplified geometry of the model assuming horizontal layering, the stochastic inversion procedure cannot explain the north-south resistivity variations in the footwall of the TFT.

Altogether, this information on both geometry and resistivity contrast suggests an apparent resistivity contrast between both sides of the fault and a constant dip angle of $\sim 70°$ over a depth ranging between ca. 5 m and ca. 40 m (Figure 7.9).

7.2.2. *Seismic tomography*

The set of final velocity models resulting from the stochastic inversion approach provides low travel-time residuals of ± 3 ms in average for most of the source-receiver pairs (Figure 7.10). This suggests that assuming simple geometry captures most of the main features of the velocity field. Furthermore, travel-time residuals show a relatively homogeneous pattern, except close to the fault trace between -5 and 15 m, where residuals abruptly increase from -5 ms to 4 ms northward. This result demonstrates that the presence of the fault influences seismic data.

Ray coverage (Figure 7.5) indicates a shallower resolution depth compared to ERT investigations. Resolution depth varies between the two sides of the fault, from ca. 8 m to ca. 5 m in the south and north, respectively. At these depths, the velocity models resulting from both the stochastic inversion (Figure 7.10) and tomography (Figure 7.5) point out high-velocity variations of about 50% at the transition of the fault zone. The 2D seismic model also emphasizes strong vertical velocity changes on both sides of the fault. High-velocity contrasts between top and bottom layers induce a concentration of rays at a depth between 2 and 4 m, which prevents deeper investigations, in particular in the north.

Taking into account this shallow investigation depth, the velocity field can be characterized by two deeper units of Vp$\sim$1100 m/s (SL) and Vp$\sim$2100 m/s (NL) below by two superficial low-velocity layers (STL: $\sim$5 m, $\sim$900 m/s and NTL: $\sim$3 m, $\sim$1600 m/s). The stochastic inversion procedure also reveals that seismic data are sensitive to the dip angle parameter (Figure 7.11). The 2D seismic inversion result suggests a

northward dipping fault with a very low-angle of ca. 20° -30° at depths down to ca. 5 m, which is consistent with field observations in the trench (Le Roux-Mallouf et al. 2020).

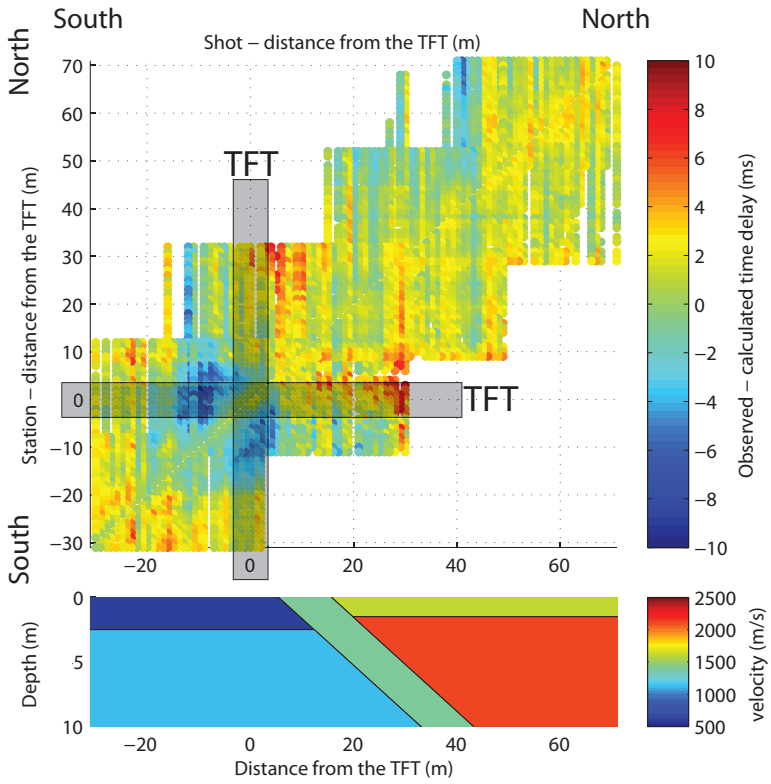

Figure 7.10. *Misfit between observed and calculated time delay corresponding to the traveltime residuals. This misfit is defined as the difference between the observed and calculated travel time using the velocity model plotted at the bottom. Compared to resistivity model (Figure 7.8), one can noted the limit of the y-axis, which corresponds to a lower depth of investigation.*

This observation is also in agreement with both ERT profile (Figure 7.3) and the related stochastic ERT results, which displays a change in dip angle with a more gentle slope of the TFT fault near the surface. Without information on the near-surface geometry of the fault, a constant fault dip angle was assumed, and the same model was used for the different ERT configurations. Thereby the inversion procedure could not image this dip angle change near the surface with resistivity data only.

Hence, seismic data inversion with field observations confirms a northward dipping fault with a low angle of ca. 20°-30° at very shallow depth. Seismic and electrical resistivity images together suggest a dip angle that increases gradually up to ca. 70° at a depth of 5-10 m.

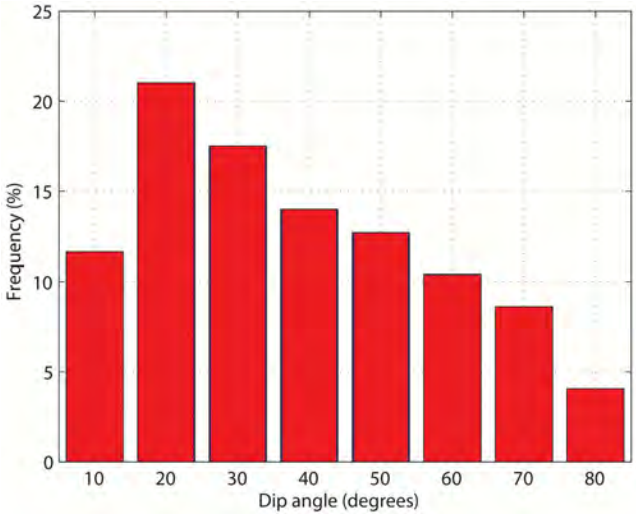

Figure 7.11. *Distribution of TFT dip angle obtained from seismic measurements.*

7.2.3. *Micro-gravity*

Since gravity measurements are affected mainly by the deeper part of the model, the focus of the study is on the long wavelength of the gravity profile associated with the two south-north gravity gradients (Figure 7.6). The result of the stochastic inversion suggests that the observed northward increase of gravity measurements is mostly related to both $\Delta\varrho$ the density contrast between SL and NL and α the fault dip angle (Figure 7.12). As indicated figure 7.12, gravity measurements cannot be used to assess the other density and geometric parameters, which remain poorly constrained.

The gravity model result reveals a tradeoff between $\Delta\varrho$ and α: the higher the density contrast, the lower the fault dip angle. For $\Delta\varrho$= -350 kg/m^3 the fault dip angle is ca. 30° , whereas for $\Delta\varrho$= -200 kg/m^3 the fault dip angle is ca. 60° (Figures 7.12a and b). This leads to a wide distribution of the fault dip angle (Figure 7.12c). The maximum obtained at $\alpha \sim$ 30-40° and the most likely model thickness down to 80 m depth suggests a fault that flattens at depths below 40 m.

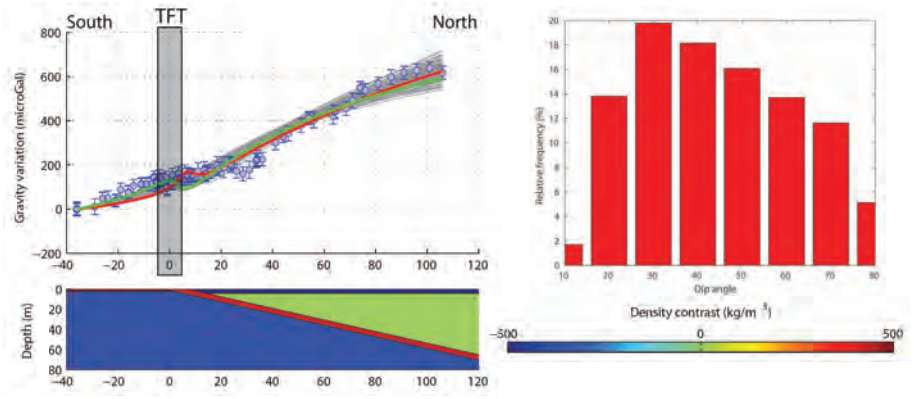

Figure 7.12. *a) Comparison between observed (blue circles) and calculated (gray lines) gravity variations along the study profile obtained for the 100 best-fitting models. b) Density contrast models associated with the red (30 ° dip angle) and green lines (60 ° dip angle) plotted above. c) Distribution of TFT dip angle obtained from gravity stochastic inversion. The red dots indicate the model with the lower misfit value.*

7.3. Implications of near-surface geophysical findings

The geometry of the fault, especially at shallow depth, is a crucial parameter for better understanding deformation kinematics and accommodation at crustal scale. In particular, the slip rate can be estimated by combining the subsurface dip angle and terrace dating results. The new constraints for the TFT geometry deduced from near-surface geophysical techniques allow studying stress partitioning at the frontal thrust zone and its associated seismic hazard implications in south Central Bhutan.

7.3.1. *Subsurface imaging*

Taking advantage of the various scales of investigation coming from ERT, seismic, and gravity methods, an accurate description of shallow structures and fault geometry at depth is obtained in the case study. The subsurface can be subdivided in three main zones:

(1) a very shallow part up to 5 m depth well-constrained by both field observations and seismic data considering the ray coverage,

(2) an intermediate depth part well-imaged by ERT sections between 5 and 40 m depth due to high resistivity contrasts,

(3) a deeper part documented by gravity measurements below 40 m depth.

The fault geometry discussed here arises from the integration of these three surface sensitivities.

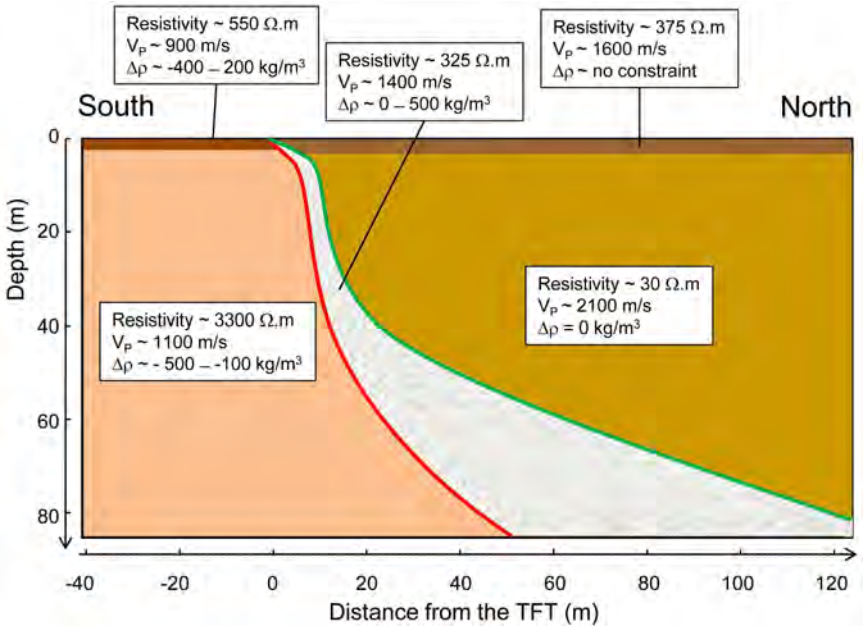

Figure 7.13. *Simplified cross section showing the main geophysical results obtained from electrical resistivity tomography, seismic refraction and gravity measurements. Together these results suggest a TFT with a flat and ramp geometry, with a surface dip angle of* $\sim 20^\circ$ *reaching* $\sim 70^\circ$ *at 20 m depth and flattening in its deeper part. Note that dashed area is bounded by the two end-member models of fault geometry given by the green and the red lines. Hence, this area does not represent the fault thickness, which is estimated to 2.5 m.*

In terms of lithological setting and water content, the geophysical datasets suggest a thin layer (∼3-5 m) that appears to be present on both sides of the fault trace and probably corresponds to recent alluvial deposits. Along the profile, resistivity and velocity variations at shallow depth may be due to a northward decrease of water saturation. Below these superficial layers, in the hanging wall of the TFT, the obtained very low-resistivity values (< 30 Ω·m), the high V_p of ca. 2100 m/s and the relatively low densities probabely underline a phyllite unit, which can be observed in the field.

Overall, the geophysical methods image a more complex fault geometry than proposed by earlier studies (Berthet et al. 2014 ; Le Roux-Mallouf et al. 2016). The geophysical results show a TFT with a flat and listric-ramp geometry with a low dip angle

of 20° -30° at shallow depth, steeply dipping at ∼70° in the middle and gradually flattening to a shallower dip angle of 30° -40° in its deeper part (Figure 7.13).

7.3.2. *Overthrusting slip rate assessment*

Berthet et al. (2014) estimated a Holocene vertical slip rate of 8.8±2.1 mm/yr by dating two uplifted river terraces in Sarpang area. Assuming a dip angle of 20-30°, a slip rate of 20.8±8.8 mm/yr, which is consistent with the GPS convergence rate of 17 mm/yr obtained across central Bhutan (Marechal et al. 2016). Finally, they conclude that the TFT mainly accommodates the Himalayan convergence. However, this major conclusion can be revisited in light of our new constraints on the TFT geometry.

First, assuming a constant overthrusting slip rate along the TFT, a vertical velocity profile is calculated from this observed uplift rate (Okada 1985). As expected, this calculated profile depends on TFT geometry: a higher fault dip angle implies a higher uplift rate. More surprisingly, it also depends on the distance between the TFT and the location of dated samples. For instance, a distance of 5 m from the TFT yields two very different vertical velocity profiles associated with the two end-member models for the fault geometry. On the contrary, if the uplift rate is measured about 10 m north from the TFT, the uplift rate difference drastically reduces. In other words, due to the flat and listric-ramp geometry of the shallow TFT, the uplift rate measured on the top of river terraces is spatially variable and cannot be constant. This result questions the validity of commonly used approaches for which a mean uplift rate is obtained by combining several uplifted terraces located at various distances from the front. Furthermore, assuming that the far-field GPS shortening rate corresponds to an upper limit for the uplift rate, our calculation shows that part of the models are unrealistic. This suggests that both the convergence rates derived from GPS and the uplift measurements can be used to reduce the *a priori* geometric parameter ranges tested in our stochastic approach.

Second, assuming no prior information on the relative location of uplift rate measurements, one can deduce the overthrusting slip rate from the TFT geometry. The slip rate associated with a rigid block model with a constant dip angle α can be easily estimated from:

$$\text{slip rate} = \frac{\text{uplift rate}}{\sin(\alpha)} \qquad [7.2]$$

As previously proposed by Berthet et al. (2014), this simple approach gives a minimum dip angle of 30° for which most of the convergence across central Bhutan is accommodated along the TFT. However, the steeper is the dip angle; the greater is the chance for slip partitioning with other faults. Assuming a constant uplift rate of 8.8±2.1 mm/yr associated with no information on the sampling location, the slip rate

can be estimated from less straightforward modeling based on the obtained geometry. In that case, using dislocations embedded in a homogeneous half-space (Okada 1985), the obtained slip rate exhibits high variations along the profile from 20-40 mm/yr above the very shallow part of the fault to 10-20 mm/yr in the northern part of the profile. Using the convergence rate as a maximum value for the slip, this result suggests a minimum distance of 8 m for the steepening of the TFT and an accommodation of at least 10 ± 2 mm/yr of the 17 mm/yr of convergence at the TFT.

The obtained uncertainties associated with this slip rate estimate arise mainly from both the location of samples for terrace dating and the fault geometry inferred from geophysical inversion.

7.3.3. *Deformation at the topographic front*

Based on new constraints on the TFT geometry and the resulting slip rate, it is proposed that at least 60% of the convergence rate due to ongoing underthrusting of India beneath the Himalaya is accommodated by the TFT.

It results that additional faults must be active in this area, which is consistent with results obtained by Dey et al. (2016) in the Kangra section of the Indian Himalayas where, besides the MFT, other out-of-sequence faulting such as the Jwalamukhi Thrust (JMT) accommodates part of the Sub-Himalayan shortening. In the case study area in south Bhutan, one can mention either the north-propagating emerging thrust front (FBT) documented by Dasgupta et al. (2013) in the Brahmaputra plain, and the Main Boundary Thrust (MBT), which accommodates the present-day deformation in eastern Bhutan (Marechal et al. 2016).

Based on recent studies, it is now well-established that at least two major earthquakes have occurred on the TFT in the past, the last one having occurred about 300 years ago in 1714 (Le Roux-Mallouf et al. 2016 ; Hetényi et al. 2016, see volume 3 chapter 5). Thus, a slip deficit of 3-5 m has accumulated on the TFT during this interseismic period, and could potentially be released in a large magnitude earthquake with high probability of rupture reaching the surface (see volume 3 – chapter 5).

Conclusion

This chapter presents high-resolution near-surface geophysical imaging results based on a joint approach, including electrical resistivity, seismic, and gravity data to constrain the TFT geometry in south Central Bhutan.

Our results show that a flat and listric-ramp geometry characterizes the upper part of the TFT with high variations of dip angle. This geometry differs from the constant

fault dip angle inferred from surface observation only. Estimating the slip rate without additional depth constraints can induce significant errors, arising from the terrace dating to determine the uplift rate and the projection of the fault dip angle based on surface observations.

By combining information from surface observations with our new constraints on the fault geometry, we estimate that at least 60% of the Himalayan convergence is accommodated by the TFT, making this fault a high seismic hazard zone.

The hypothesis of slip partitioning cannot be totally ruled out. Other faults such as the FBT emerging in the Brahmaputra plain, and the MBT can also be active. Therefore, further studies combining geomorphology and near-surface geophysics along the Himalayan front, especially towards the eastern part of Bhutan, will be helpful to study potential lateral variations in the fault geometry and its implication on the present-day strain partitioning. Moreover, local variability across the TFT may be assessed by exploring areas within a few 100s of meters along strike with respect to the Sarpang study area.

Bibliography

Berthet, T., Ritz, J. F., Ferry, M., Pelgay, P., Cattin, R., Drukpa, D., Braucher, R., Hetényi, G. (2014). Active tectonics of the eastern Himalaya: New constraints from the first tectonic geomorphology study in southern Bhutan, Geology, 42(5), 427–430.

Binley, A. (2015). Tools and Techniques: Electrical Methods, Vol. 11, Elsevier B.V.

Binley, A., Kemna, A. (2005). Electrical Methods, p. 129-156. In Hubbard, S., Rubin,Y. (eds.), Hydrogeophysics. Springer.

Boness, N. L., Zoback, M. D. (2004). Stress-induced seismic velocity anisotropy and physical properties in the SAFOD Pilot Hole in Parkfield, CA, Geophysical Research Letters, 31 (15).

Cattin, R., Mazzotti, S., Baratin, L. M. (2015). GravProcess: An easy-to-use MATLAB software to process campaign gravity data and evaluate the associated uncertainties, Computers and Geosciences, 81, 20–27.

Dahlin, T., Zhou, B. (2004). A numerical comparison of 2D resistivity imaging with 10 electrode arrays, Geophysical Prospecting, 52(5), 379–398.

Dasgupta, S., Mazumdar, K., Moirangcha, L. H., Gupta, T. D., Mukhopadhyay, B. (2013). Seismic landscape from Sarpang re-entrant, Bhutan Himalaya foredeep, Assam, India: Constraints from geomorphology and geology, Tectonophysics, 592, 130–140.

Demanet, D., Pirard, E., Renardy, F., Jongmans, D. (2001). Application and processing of geophysical images for mapping faults, Computers and Geosciences, 27(9), 1031–1037.

Dey, S., Thiede, R. C., Schildgen, T. F., Wittmann, H., Bookhagen, B., Scherler, D., Strecker, M. R. (2016). Holocene internal shortening within the northwest Sub-Himalaya: Out-of-sequence faulting of the Jwalamukhi Thrust, India, Tectonics, 35(11), 2677–2697.

Drukpa, D., Stephanie, G., Rodolphe, C., Kinley, N., Nicolas, L. M. (2017). Impact of near-surface fault geometry on secular slip rate assessment derived from uplifted river terraces: Implications for convergence accommodation across the frontal thrust in southern Central Bhutan, Geophysical Journal International, 212(2), 1315–1330. .

Ellis, R. G., Oldenburg, D. W. (1994). Applied geophysical inversion, Geophysical Journal International, 116(1), 5–11.

Gelis, C., Revil, A., Cushing, M., Jougnot, D., Lemeille, F., Cabrera, J., de Hoyos, A., Rocher, M. (2010), 'Potential of electrical resistivity tomography to detect fault zones in limestone and argillaceous formations in the experimental platform of tournemire, france', Pure and Applied Geophysics, 167, 1405–1418.

Hammer, P., Berthet, T., Hetényi, G., Cattin, R., Drukpa, D., Chophel, J., Lechmann, S., Moigne, N. L., Champollion, C., Doerflinger, E. (2013). Flexure of the India plate underneath the Bhutan Himalaya, Geophysical Research Letters, 40(16), 4225–4230.

Hetényi, G., Cattin, R., Berthet, T., Le Moigne, N., Chophel, J., Lechmann, S., Hammer, P., Drukpa, D., Sapkota, S. N., Gautier, S. , Thinley, K. (2016). Segmentation of the Himalayas as revealed by arc-parallel gravity anomalies, Scientific Reports, 6 (September), 33866.

Hung, J.-H., Ma, K.-F., Wang, C.-Y., Ito, H., Lin, W., Yeh, E.-C. (2009). Subsurface structure, physical properties, fault-zone characteristics and stress state in scientific drill holes of Taiwan Chelungpu Fault Drilling Project, Tectonophysics, 466(3), 307–321.

Jeppson, T. N., Bradbury, K. K., Evans, J. P. (2010). Geophysical properties within the San Andreas Fault Zone at the San Andreas Fault Observatory at Depth and their relationships to rock properties and fault zone structure, Journal of Geophysical Research: Solid Earth, 115(B12).

Kaiser, A. E., Green, A. G., Campbell, F. M., Horstmeyer, H., Manukyan, E., Langridge, R. M., McClymont, A. F., Mancktelow, N., Finnemore, M. , Nobes, D. C. (2009). Ultrahigh-resolution seismic reflection imaging of the Alpine Fault, New Zealand, Journal of Geophysical Research: Solid Earth, 114(11), 1–15.

Le Roux-Mallouf, R., Ferry, M., Cattin, R., Ritz, J., , Drukpa, D. (submitted). A 2600-yr-long paleoseismic record for the Himalayan Main Frontal Thrust (Western Bhutan), Solid Earth, 11, 2359–2375

Le Roux-Mallouf, R., Ferry, M., Ritz, J.-f., Berthet, T., Cattin, R. , Drukpa, D. (2016). First paleoseismic evidence for great surface-rupturing earthquakes in the Bhutan Himalayas, Journal of Geophysical Research: Solid Earth, 121(10), 7271–7283.

Loke, M., Barker, R. D. (1996). Rapid least-squared inversion of apparent resisitivity pseudosections by a quasi-Newton method, Geophysical prospecting, 44(1), 131–152.

Loke, M. H. (2015). Tutorial : 2-D and 3-D electrical imaging surveys, Geotomo Software Malaysia, (July), 176.

Long , McQuarrie, N., Tobgay, T., Grujic, D., Hollister, L. (2011). Geologic map of Bhutan, Journal of Maps, 7(1), 184–192.

Louis, I. F., Raftopoulos, D., Goulis, I., Louis, F. I. (2002). Geophysical imaging of faults and fault zones in the urban complex of Ano Liosia neogene basin, Greece: synthetic simulation approach and field investigation, International Conference on Earth Sciences and Electronics, 2002, (October), 269–285.

Marechal, A., Mazzotti, S., Cattin, R., Cazes, G., Vernant, P., Drukpa, D., Thinley, K., Tarayoun, A., Roux-Mallouf, L., Thapa, B. B. et al. (2016). Evidence of interseismic coupling variations along the bhutan himalayan arc from new GPS data, Geophysical Research Letters, 43, doi:10.1002/2016GL071163.

Morandi, S., Ceragioli, E. (2002), Integrated interpretation of seismic and resistivity images across the «Val d'Agri» graben (Italy), Annals of Geophysics, 45(2).

Mosegaard, K., Tarantola, A. (1995). Monte Carlo sampling of solutions to inverse problems, Journal of Geophysical Research: Solid Earth, 100(B7), 12431–12447.

Mussett, A., Khan, M., Button, S. (2000). Looking Into the Earth: An Introduction to Geological Geophysics, Cambridge University Press.

Nguyen, F. (2005). Near-surface Geophysical Imaging and Detection of Slow Active Faults, Department of Georessources, Geotechnologies and Construction Materials, Doctorate, (May), 359.

Nguyen, F., Garambois, S., Chardon, D., Hermitte, D., Bellier, O., Jongmans, D. (2007). Subsurface electrical imaging of anisotropic formations affected by a slow active reverse fault, Provence, France, Journal of Applied Geophysics, 62(4), 338–353.

Nguyen, F., Garambois, S., Jongmans, D., Pirard, E., Loke, M. H. (2005). Image processing of 2D resistivity data for imaging faults, Journal of Applied Geophysics, 57(4), 260–277.

Okada, Y. (1985). Surface deformation due to shear and tensile faults in a half-space, Bulletin of the seismological society of America, 75(4), 1135–1154.

Pasquet, S., Bodet, L., Dhemaied, A., Mouhri, A., Vitale, Q., Rejiba, F., Flipo, N., Guérin, R. (2015), 'Detecting different water table levels in a shallow aquifer with combined p-, surface and sh-wave surveys: Insights from vp/vs or poisson's ratios', Journal of Applied Geophysics, 113, 38–50.

Phillips, W. J., Kuckes, A. F. (1983). 'Electrical conductivity structure of the san andreas fault in central california', Journal of Geophysical Research: Solid Earth, 88(B9), 7467–7474.

Podvin, P., Lecomte, I. (1991). 'Finite difference computation of traveltimes in very contrasted velocity models: a massively parallel approach and its associated tools', Geophysical Journal International, 105(1), 271–284.

Priolo, E., Lovisa, L., Zollo, A., Böhm, G., D'Auria, L., Gautier, S., Gentile, F., Klin, P., Latorre, D., Michelini, A. et al. (2012). The Campi Flegrei Blind Test: Evaluating the Imaging Capability of Local Earthquake Tomography in a Volcanic Area, International Journal of Geophysics, 2012.

Ramirez, A. L., Nitao, J. J., Hanley, W. G., Aines, R., Glaser, R. E., Sengupta, S. K., Dyer, K. M., Hickling, T. L., Daily, W. D. (2005). Stochastic inversion of electrical resistivity changes using a Markov Chain Monte Carlo approach, Journal of Geophysical Research: Solid Earth, 110(B2).

Reynolds, J. (1997). An Introduction to Applied and Environmental Geophysics, John Wiley.

Schuster, G. T. (1993). Wavepath eikonal traveltime inversion: Theory, Geophysics, 58(9), 1314.

Sheehan, J. R., Doll, W. E., Mandell, W. a. (2005). An Evaluation of Methods and Available Software for Seismic Refraction Tomography Analysis, Journal of Environmental & Engineering Geophysics, 10(1), 21–34.

Suzuki, K., Toda, S., Kusunoki, K., Fujimitsu, Y., Mogi, T., Jomori, A. (2000). 'Case studies of electrical and electromagnetic methods applied to mapping active faults beneath the thick quaternary', Engineering Geology, 56(1), 29–45.

Tarantola, A. (2005). Inverse problem theory and methods for model parameter estimation, Society for Industrial and Applied Mathematics.

Telford, W. M., Geldart, L. P., Sheriff, R. E. (1990). Applied geophysics, Vol. 1, Cambridge university press.

Villani, F., Tulliani, V., Sapia, V., Fierro, E., Civico, R., Pantosti, D. (2015). Shallow subsurface imaging of the Piano di Pezza active normal fault (central Italy) by high-resolution refraction and electrical resistivity tomography coupled with time-domain electromagnetic data, Geophysical Journal International, 203(3), 1482–1494.

Won, I.J., Bevis, M. (1987). Computing the gravitational and magnetic anomalies due to a polygon: Algorithms and Fortran subroutines, Geophysics, 52(2), 232–238.

Wise, D. J., Cassidy, J., Locke, C. A. (2003). Geophysical imaging of the Quaternary Wairoa North Fault, New Zealand: A case study, Journal of Applied Geophysics, 53(1), 1–16.